Journal of Solid State Chemistry 184 (2011) 81–88

Contents lists available at ScienceDirect

Journal of Solid State Chemistry

journal homepage: www.elsevier.com/locate/jssc

Synthesis, structures and photocatalytic activities of microcrystalline $ABi_2Nb_2O_9$ (A=Sr, Ba) powders

Weiming Wu, Shijing Liang, Xiaowei Wang, Jinhong Bi, Ping Liu, Ling Wu *

State Key Laboratory Breeding Base of Photocatalysis, Research Institute of Photocatalysis, Fuzhou University, Fuzhou 350002, PR China

ARTICLE INFO

Article history:
Received 10 April 2010
Received in revised form
19 October 2010
Accepted 26 October 2010
Available online 3 November 2010

Keywords:
Citrate complex
Microcrystalline
$ABi_2Nb_2O_9$ (A=Sr, Ba)
Photocatalysis

ABSTRACT

Microcrystalline $ABi_2Nb_2O_9$ (A=Sr, Ba) photocatalysts were successfully synthesized by a citrate complex method. The as-prepared samples were characterized by the X-ray diffraction technique, BET surface area analysis, UV–vis diffuse reflectance spectrum, transmission electron microscopy, X-ray photoelectron spectroscopy and inductively coupled plasma-atomic emission spectrometry. The results indicated that single-phase orthorhombic $SrBi_2Nb_2O_9$ could be obtained after being calcined above 650 °C, while $BaBi_2Nb_2O_9$ was tetragonal. Based on the diffuse reflectance spectra, the band gaps of the obtained samples were calculated to be around 3.34–3.54 eV. For the photocatalytic redox reaction of methyl orange under UV-light irradiation, $SrBi_2Nb_2O_9$ exhibited higher photocatalytic activity than that of $BaBi_2Nb_2O_9$. The effects of the crystallinities, BET surface areas and crystal structures of the samples on the photocatalytic activities were discussed in detail.

1. Introduction

An increasing interest in Aurivillius-type compounds with a general formula $(Bi_2O_2)^{2+}$ $(A_{n-1}B_nO_{3n+1})^{2-}$ has developed during latest years, because of their possible use as nonvolatile ferroelectric memories and high temperature piezoelectrics [1]. Meanwhile, a series of Aurivillius-type photocatalysts has also attracted much attention, Bi_2AO_6 (A=Mo, W) [2–6], Bi_3TiNbO_9 [7], $PbBi_2Nb_2O_9$ [8,9], $LiBi_4M_3O_{14}$ (M=Nb, Ta) [10] and so on. Recently, Li and his co-workers [11] have found Aurivillius-type $ABi_2Nb_2O_9$ (A=Sr, Ba) powders obtained by the conventional solid state reaction can split water into H_2 and O_2 under UV-light irradiation.

Until now, various methods have been employed to synthesized Aurivillius-type compounds, such as solid state reaction [8,10–12], ultrasonic-assisted method [13], molten salt process [14], sol–gel method [7,9] and solvent-thermal route [2,15]. $ABi_2Nb_2O_9$ (A=Sr, Ba), which as members of the quaternary system compounds of Aurivillius, are usually prepared by the solid state reaction [11,16,17], because impure samples are often obtained by other methods (such as solvent-thermal route). However, the introduction of the conventional solid state reaction which generally requires a repeated mechanical mixing and a high-temperature process often gives rise to particles agglomeration with severe loss of effective surface area. Thus, it is necessary to develop a time-saving method to synthesize $ABi_2Nb_2O_9$ (A=Sr, Ba) powders at a relatively low temperature. A sol–gel synthesis [18] and a co-precipitation method [19,20] have been applied to synthesize $ABi_2Nb_2O_9$ (A=Sr, Ba) powders at a relatively low calcination temperature. However, the sol–gel method has great difficulty in obtaining $ABi_2Nb_2O_9$ (A=Sr, Ba) powders, because of the instability of starting materials in water, such as niobium ethoxide [18]. Moreover the aqueous solutions of niobium obtained by chemical processes [21–23] are complicated due to scarcity of water-soluble compounds for niobium and easy hydrolysis of the available ones (such as $NbCl_5$). Thus, a citrate complex method developed for the preparation of $ABi_2Nb_2O_9$ (A=Sr, Ba) powders has been reported by some workers [24–26]. Starting from a peroxo-citrato-niobium precursor solution, this method offers a low-cost, environmentally friendly alternative to the conventional sol–gel technique.

In this paper, Microcrystalline $ABi_2Nb_2O_9$ (A=Sr, Ba) photocatalysts were successfully synthesized by a citrate complex method. The photocatalytic activities of the obtained samples were evaluated by the photocatalytic redox reaction of methyl orange (MO) in the aqueous solution for the first time. $SrBi_2Nb_2O_9$ (SBN) and $BaBi_2Nb_2O_9$ (BBN) exhibited different performances in the catalytic test. It was also observed that samples obtained at different calcination temperatures showed different photocatalytic activities. The as-prepared samples were characterized by several techniques, and the effects of the crystallinities, BET surface areas and crystal structures of the samples on the photocatalytic activities were discussed in detail.

2. Experimental

2.1. Materials and reagents

The following materials and reagents were used as starting materials: citric acid monohydrate ($C_6H_8O_7 \cdot H_2O$, A.R., Sinopharm Chemical Reagent Co. (SCRC)), ammonia (p.a. NH_3 ca. 25% in H_2O, SCRC), nitric acid (HNO_3, 65–68 wt%, SCRC), niobium

* Corresponding author. Fax: +86 591 83779105.
E-mail address: wuling@fzu.edu.cn (L. Wu).

0022-4596/$ - see front matter © 2010 Elsevier Inc. All rights reserved.
doi:10.1016/j.jssc.2010.10.033

ammonium oxalate ($NH_4H_2[NbO(C_2O_4)_3]\cdot 3H_2O$, 20.7% in Nb, H.C. Starck), hydrogen peroxide (H_2O_2, 30 wt% solution in water, SCRC), strontium nitrate ($Sr(NO_3)_2$, A.R., SCRC), barium nitrate ($Ba(NO_3)_2$, A.R., SCRC) and bismuth nitrate pentahydrate ($Bi(NO_3)_3\cdot 5H_2O$, A.R., SCRC). Deionized water was used in the whole experiment.

2.2. Preparation of a peroxo-citrato-niobium precursor solution

The peroxo-citrato-niobium precursor solution was prepared by a synthesis route similar to the earlier work reported by Narendar and Messing [27]: citric acid monohydrate (10 mmol, 2.10 g) was dissolved in 15.0 mL hydrogen peroxide. A 1.0 mL nitric acid was added into this solution. After niobium ammonium oxalate (5 mmol, 2.24 g) was added, the resulting solution was stirred at 65 °C for 1 h to ensure complete oxalate decomposition. Then, the pH value was slowly raised to 6.5 by adding ammonia.

2.3. Preparation of a strontium–bismuth–citrate solution

$Sr(NO_3)_2$ (2.5 mmol, 0.53 g), $Bi(NO_3)_3\cdot 5H_2O$ (5 mmol, 2.42 g) and citric acid monohydrate (15 mmol, 3.15 g) were dissolved in 20.0 mL deionized water. An ammonia solution was added to this solution until the pH of the solution was up to 6.5 to obtain a colorless strontium–bismuth–citrate solution.

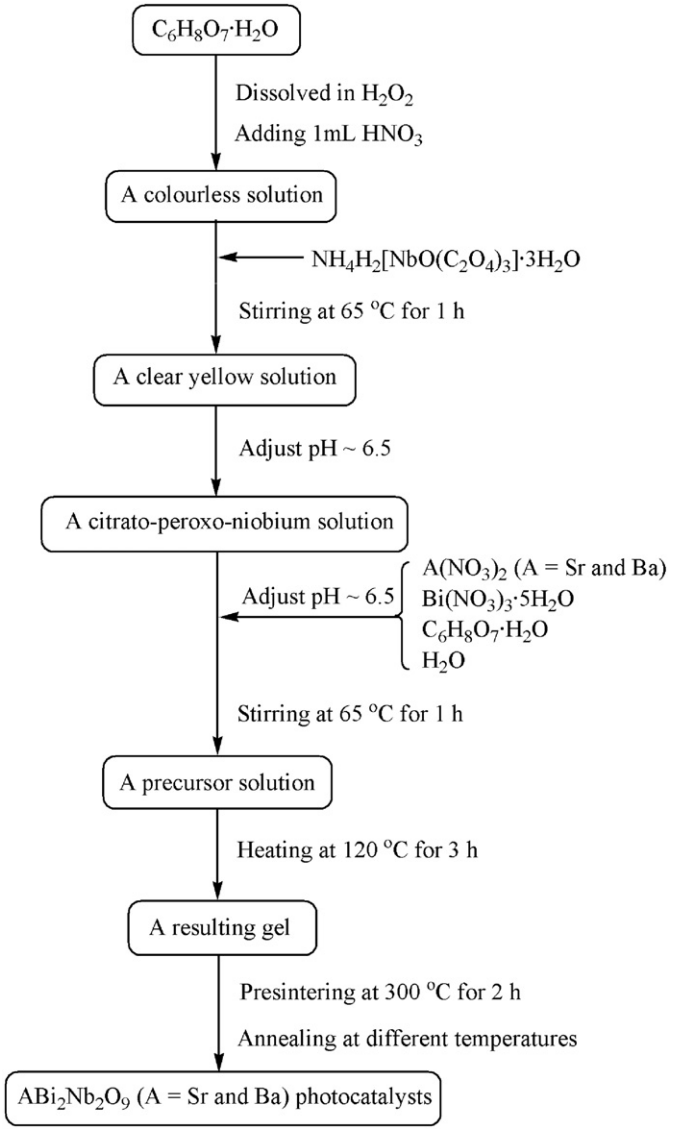

Fig. 1. The flowchart of the citrate complex method used to prepare $ABi_2Nb_2O_9$ (A=Sr, Ba) powders.

2.4. Preparation of $SrBi_2Nb_2O_9$ photocatalysts

The peroxo-citrato-niobium precursor solution and strontium–bismuth–citrate solution were mixed homogeneously in stoichiometric ratio and then heated at 65 °C for 1 h. As water evaporated, the solution turned into a gel with a high viscosity. The gel was heated at 300 °C for 2 h to remove organic compounds and then calcined at 650, 750 and 850 °C for 4 h. The as-prepared samples were denoted as SBN-650, SBN-750 and SBN-850, corresponding to the products obtained at 650, 750 and 850 °C, respectively.

2.5. Preparation of $BaBi_2Nb_2O_9$ photocatalysts

The BBN photocatalysts were also prepared by the citrate complex method with niobium ammonium oxalate, $Bi(NO_3)_3\cdot 5H_2O$ and

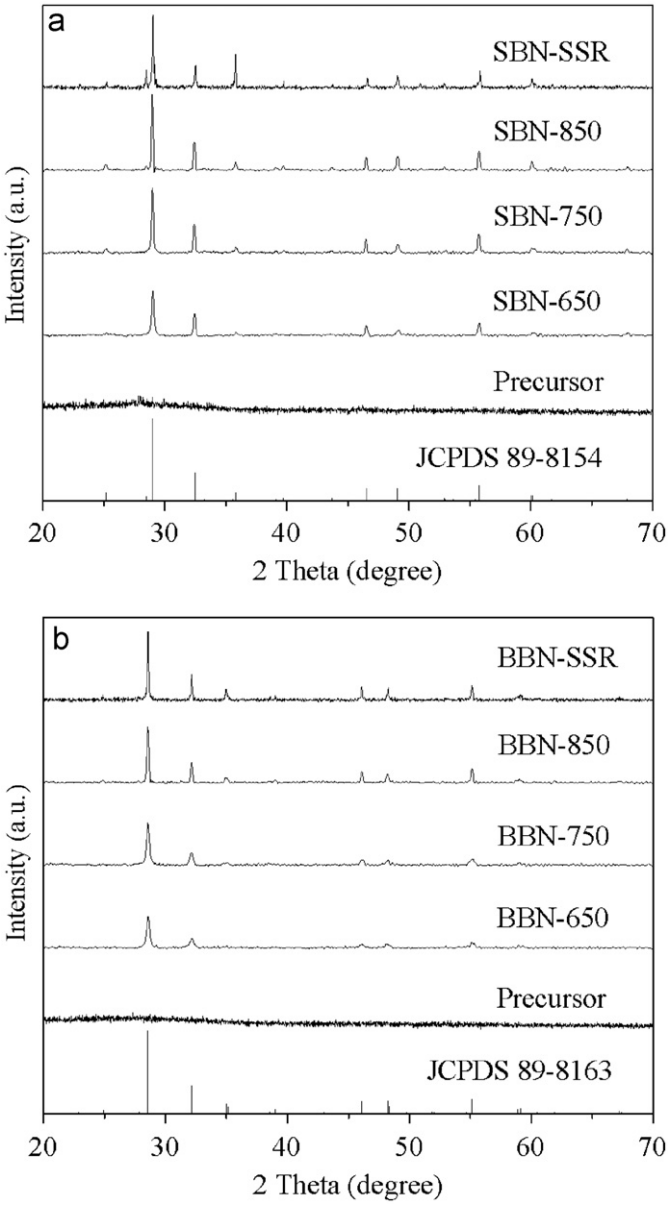

Fig. 2. XRD patterns of the samples prepared by the citrate complex method: (a) SBN and (b) BBN.

$Ba(NO_3)_2$ as precursors. The BBN samples obtained at 650, 750 and 850 °C were denoted as BBN-650, BBN-750 and BBN-850, respectively. The flowchart of the citrate complex method used to prepare $ABi_2Nb_2O_9$ (A=Sr, Ba) powders was presented in Fig. 1.

Table 1
Preparation conditions, BET surface areas and band gaps of microcrystalline $ABi_2Nb_2O_9$ (A=Sr, Ba) samples synthesized by the citrate complex method and the solid state reaction.

Sample	Condition	BET (m^2/g)	E_g (eV)
SBN-650	650 °C, 4 h	6.9	3.54
SBN-750	750 °C, 4 h	3.5	3.51
SBN-850	850 °C, 4 h	2.2	3.48
SBN-SSR	Solid state reaction	1.7	3.44
BBN-650	650 °C, 4 h	6.5	3.51
BBN-750	750 °C, 4 h	3.3	3.46
BBN-850	850 °C, 4 h	1.9	3.39
BBN-SSR	Solid state reaction	1.2	3.34

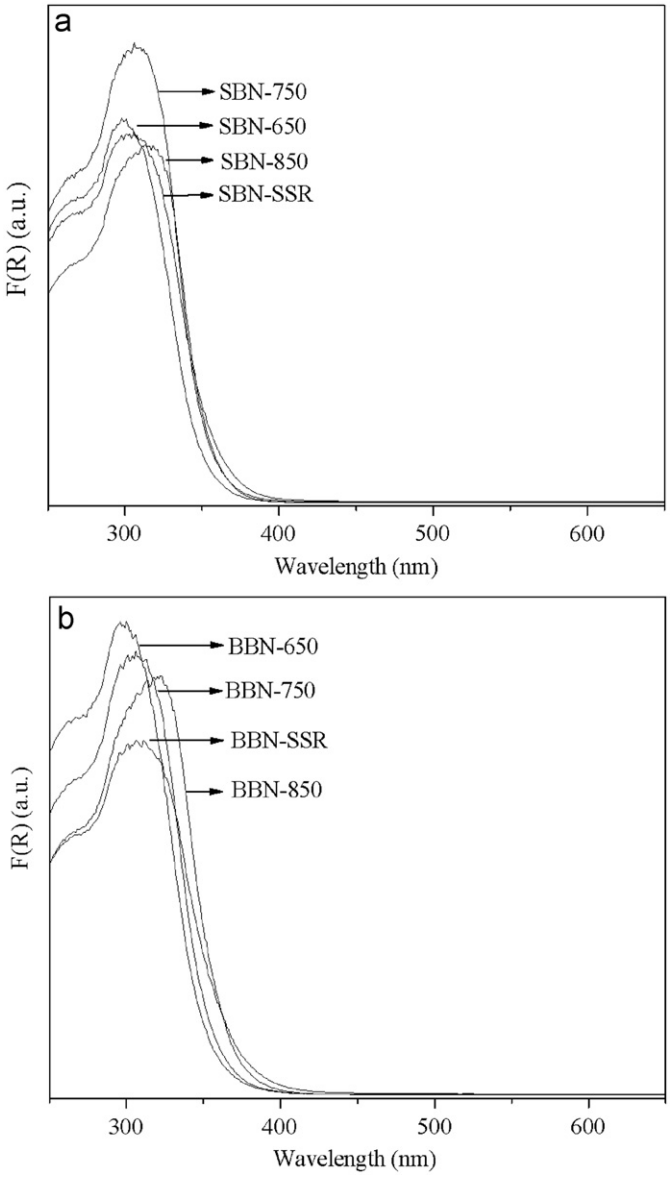

Fig. 3. Kubelka-Munk absorption function spectra of (a) SBN and (b) BBN.

2.6. Solid state reaction of $ABi_2Nb_2O_9$ (A=Sr, Ba) photocatalysts

For comparison, $ABi_2Nb_2O_9$ (A=Sr, Ba) photocatalysts were also prepared by the solid state reaction [11]. A mixture of $SrCO_3$, $BaCO_3$, Bi_2O_3 and Nb_2O_5 with an appropriate molar ratio was calcined at 900 °C for 15 h, 1000 °C for 15 h and 1200 °C for 24 h with intermittent grinding for SBN and 1000 °C for 72 h for BBN. The samples were denoted as SBN-SSR and BBN-SSR for SBN and BBN, respectively.

2.7. Characterizations

X-ray diffraction (XRD) patterns were collected on a Bruker D8 Advance X-ray diffractometer with Cu $K\alpha$ radiation. The data were

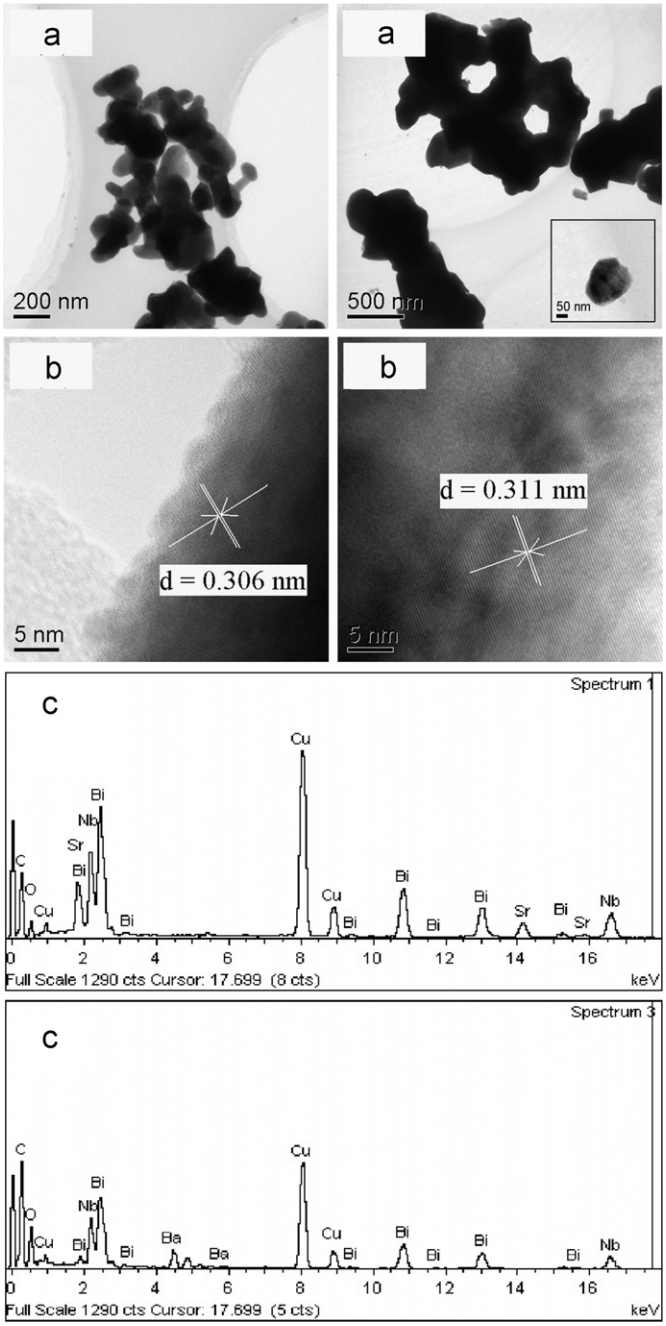

Fig. 4. TEM, HRTEM images and EDS spectra of SBN-750 and BBN-850.

recorded in the 2θ range of 20–70°. The UV–vis diffuse reflectance spectra (UV–vis DRS) were obtained on a Cary 500 UV–vis-NIR spectrophotometer (Varian Co.). $BaSO_4$ was used as a reflectance standard. The spectra were converted by the instrument software to $F(R)$ values according to Kubelka-Munk method [$F(R)=(1-R)^2/2R$]. Brunauer–Emmett–Teller (BET) surface area was measured with an ASAP2020M apparatus (Micromeritics Instrument Co.). Before the test, the as-prepared sample was degassed in a quartz tube at 200 °C for 2 h. The transmission electron microscopy (TEM) and high-resolution transmission electron microscopy (HRTEM) images were measured by a JEOL JEM-2010 transmission electron microscope equipped with an energy-dispersive X-ray spectroscope (EDS) at an accelerating voltage of 200 kV. Samples for TEM were prepared by placing a drop of the sample suspension on a copper grid coated with carbon film and dried in the atmosphere. X-ray photoelectron spectroscopy (XPS) measurements were carried out by using a VG Scientific ESCA Lab Mark II spectrometer equipped with an Mg X-ray source ($h\upsilon=1253.6$ eV). The binding energy (BE) calibration of the spectra has been referred to C 1s peak located at BE=284.4 eV for the analysis. Further, the metal contents were determined by inductively coupled plasma-atomic emission spectrometry (ICP-AES) on an Ultima 2 inductively coupled plasma OES spectrometer (Jobin Yvon Co.).

Table 2
Stoichiometric and experimental ratio of metal elements by mass for $ABi_2Nb_2O_9$ (A=Sr, Ba).

Sample	Sr (wt%)	Ba (wt%)	Bi (wt%)	Nb (wt%)
SBN-650	9.43	–	51.82	23.26
SBN-750	10.06	–	51.96	23.53
SBN-850	9.87	–	51.17	22.04
SBN[a]	10.49	–	50.03	22.24
BBN-650	–	14.36	51.26	22.20
BBN-750	–	14.73	51.24	22.93
BBN-850	–	13.92	50.51	22.52
BBN[a]	–	15.52	47.22	20.99

[a] The stoichiometric ratio of metal elements by mass for $ABi_2Nb_2O_9$ (A=Sr, Ba).

2.8. Photocatalytic test

The photodegradation of MO catalyzed by the $ABi_2Nb_2O_9$ (A=Sr, Ba) samples was investigated under UV-light irradiation. Three 4 W ultraviolet lamps ($\lambda=254$ nm, Philips Co.) were used as the illumination source. The catalyst (160 mg) was suspended in an MO solution (160 mL, 10 mg/L) in a quartz tube. Before the irradiation, a time period of an hour was allowed to ensure the establishment of adsorption/desorption equilibrium between the catalyst and MO. As the reaction proceeded, a 3 ml suspension was taken at 20 min intervals during the catalytic reaction and was centrifuged. The MO concentrations during the degradation were analyzed by measuring the absorbance at 464 nm with a Cary 50 UV–vis spectrophotometer (Varian Co.). The whole photocatalytic process was carried out under O_2 bubbling with the flow rate of 30 mL/min.

For the photocatalytic reduction of MO, 80 mg of the sample was dispersed in 160 mL MO solution (20 mg/L). After an 80 mg ammonium oxalate was added, the suspension was stirred in the dark for 1 h to ensure the establishment of absorption/desorption equilibrium, and then irradiated using UV-light ($\lambda=254$ nm) under N_2 bubbling with the flow rate of 60 mL/min. A 3 ml suspension was taken at 10 min intervals for the UV–vis spectrum analysis. For comparison, the photocatalytic reduction of MO by Degussa P25 was performed according to the same procedure.

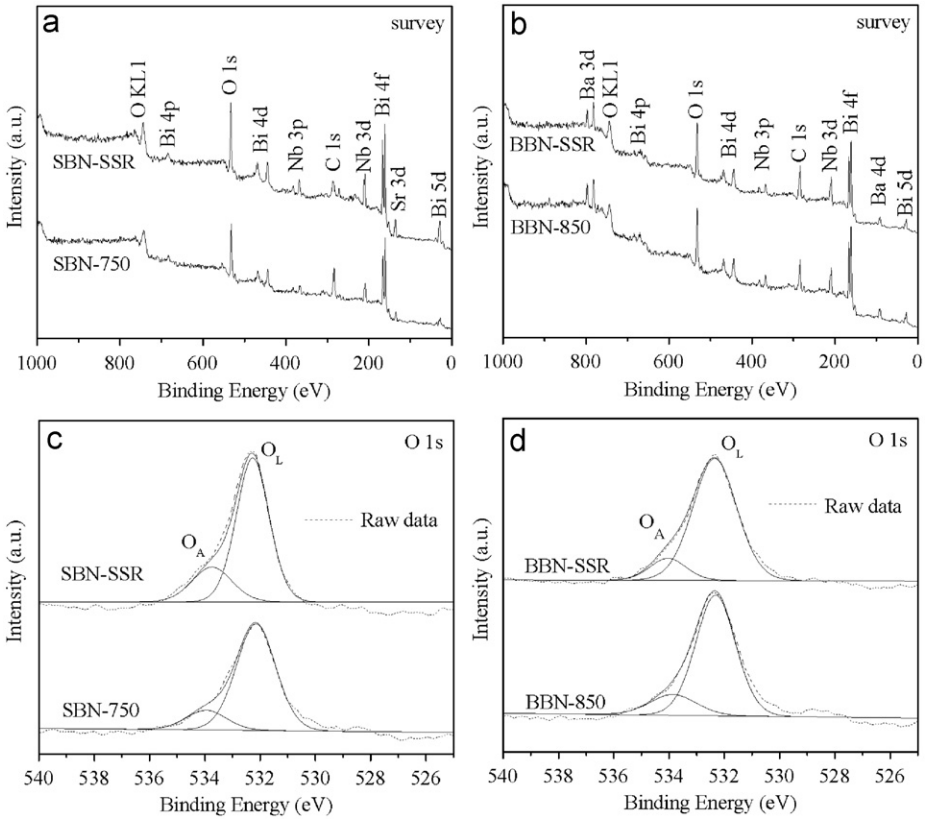

Fig. 5. XPS survey patterns of (a) SBN and (b) BBN and high resolution XPS spectra of O 1s for (c) SBN and (d) BBN.

3. Results and discussion

3.1. XRD and BET surface area

The phases and compositions of the samples were investigated by using the XRD measurement. XRD patterns of the samples prepared via the citrate complex method and the solid state reaction are shown in Fig. 2. All the diffraction peaks are well-indexed with orthorhombic ($A2_1am$) SBN and tetragonal ($I4_1/mmm$) BBN according to the JCPDS card No. 89-8154 for SBN and No. 89-8163 for BBN, respectively. No second phase is detected for all samples. It is observed that Aurivillius-type $ABi_2Nb_2O_9$ (A=Sr, Ba) can be obtained by annealing at temperatures as low as 650 °C. This temperature is much lower than that prepared by the solid state reaction as reported for the formation of $ABi_2Nb_2O_9$ (A=Sr, Ba). Note that the intensity of diffraction peaks becomes sharper at higher temperatures, indicating that the crystallinities of $ABi_2Nb_2O_9$ (A=Sr, Ba) increase with the increase of the calcination temperature. It is also found that the BET surface areas of the as-prepared samples (see Table 1) decrease with the increasing calcination temperature. This result can be explained by the increase of the particle size and the particle agglomeration occurred at high calcination temperatures.

3.2. UV–vis DRS

Kubelka-Munk absorption function F(R) spectra of the calcined powders are shown in Fig. 3. The wavelength at the absorption edge, λ, is determined as the intercept on the wavelength axis for a tangential line drawn on the absorption spectra. It can be seen that the absorption edges of the as-prepared samples locate at about 365 nm, corresponding to band gaps of *ca.* 3.4 eV. The band gaps (E_g) of the samples are calculated and are summarized in Table 1. With the increasing calcination temperature, the as-prepared samples show a slight red-shift in the band gap transition. The red-shift can be ascribed to the increase of particle size, which agrees with the result of the BET analysis. Furthermore, an intense absorption band with a steep edge is observed. This indicates that the absorption band is induced by the band gap transition instead of the transition from impurity levels [28]. For $ABi_2Nb_2O_9$ (A=Sr, Ba), Sr and Ba ions construct the crystal structures as A site cations in perovskite compounds, but they do not directly contribute to the band formation [29]. The valence bands can be mainly composed of O 2p orbitals, when orbitals of Bi 6p in Bi^{3+} may take part in the formation of the conduction bands with Nb 4d orbitals.

3.3. Morphology

The morphologies of SBN-750 and BBN-850 were investigated by TEM. Particle agglomeration is observed by TEM because of the sintering process (Fig. 4 (a)). HRTEM images (Fig. 4 (b)) show clear lattice fringes. Note that the d=0.306 nm of lattice fringes match that of the (1 1 5) crystallographic plane of an SBN, while the lattice spacing of d=0.311 nm correspond to the (1 0 5) plane of the BBN crystal. The EDS results (Fig. 4(c)) demonstrate that all peaks on the curve can be ascribed to Sr (Ba for BBN), Bi, Nb, O, Cu and C elements and no peaks with other elements are observed. The presence of Cu and C comes from copper grid and carbon film, which commonly exist for TEM. Therefore, it can be concluded that all samples are composed of Sr (Ba for BBN), Bi, Nb and O only. Furthermore, as shown in Table 2, the metal contents in the as-prepared samples obtained by an ICP-AES can be compared well with the stoichiometric ratio of metal elements by mass for $ABi_2Nb_2O_9$ (A=Sr, Ba).

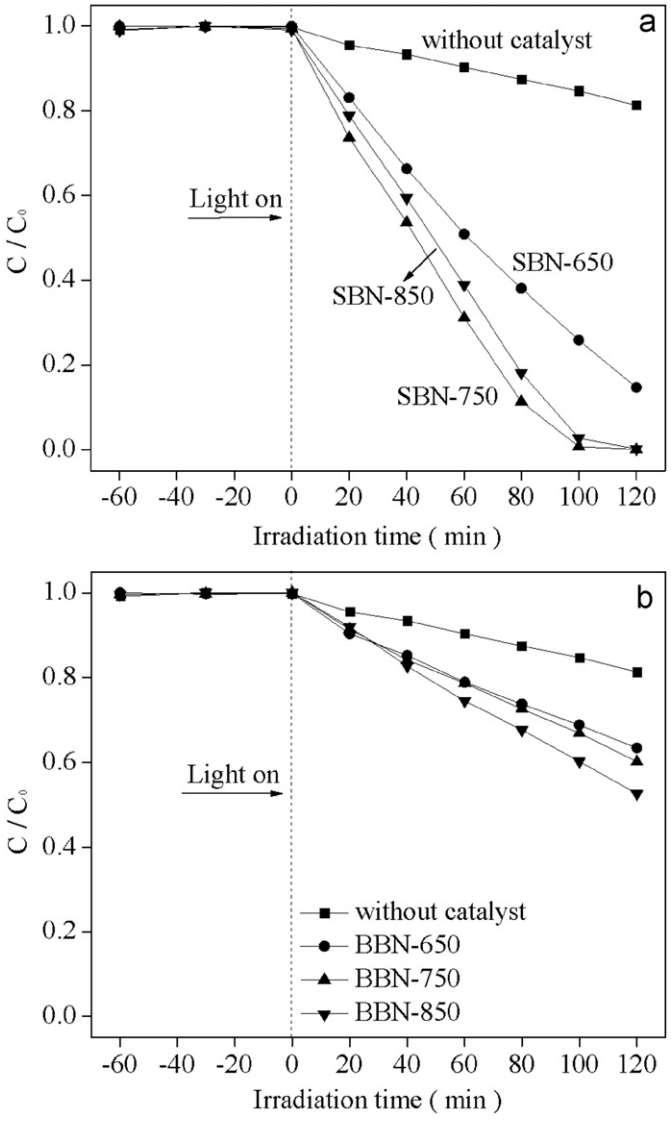

Fig. 6. Concentration changes of MO at 464 nm as a function of irradiation time during the degradation process under UV-light irradiation: (a) SBN and (b) BBN.

Table 3
BE values of the main peaks and relative composition of the samples investigated.

Sample	O 1s		Sr $3d_{5/2}$ (eV)	Ba $3d_{5/2}$ (eV)	Bi $4f_{7/2}$ (eV)	Nb $3d_{5/2}$ (eV)
	O_L (eV)	O_A (eV)				
SBN-750	532.2	534.0	135.0	–	161.4	209.1
SBN-SSR	532.3	534.2	135.2	–	161.4	209.1
BBN-850	532.4	534.4	–	781.8	161.5	209.2
BBN-SSR	532.4	533.7	–	782.2	161.5	209.2

3.4. XPS

Surface chemical compositions of the as-prepared samples (SBN-750, SBN-SSR, BBN-850 and BBN-SSR) were studied by an XPS. The XPS survey spectra of the samples and the high resolution XPS spectra of O 1s for the samples are shown in Fig. 5. The values of binding energy (BE) and relative chemical composition of the samples are reported in Table 3. All peaks on the survey spectra can be ascribed to Sr (Ba for BBN), Bi, Nb, C and O elements and no peaks with others elements are observed. The carbon element comes from the hydrocarbon contaminants, which commonly exist for an XPS. As shown in Table 3, the binding energies of an Sr $3d_{5/2}$, Ba $3d_{5/2}$, Bi $4f_{7/2}$, Nb $3d_{5/2}$ and O1s in the $ABi_2Nb_2O_9$ (A=Sr, Ba) samples obtained by the citrate complex method and the solid state reaction have no obvious changes in their position. The O1s spectra of the samples (Figs. 5 (c) and (d)) are composed of two lines: the main peak at ~532.2 eV is assigned to the lattice oxygen (O_L), and the binding energy peak at ~534.0 eV can be attributed to the loosely bound oxygen (O_A), such as an adsorbed O_2 and adsorbed H_2O. The binding energy of Sr $3d_{5/2}$ (~135.1 eV) agrees well with the binding energy of bulk SrO [30]. Note that the BE of Ba $3d_{5/2}$ (~782.0 eV) is higher than that of BaO (779.6 eV), but it is consistent with the BE value quoted for Ba $3d_{5/2}$ (781.6 eV) in $BaSO_4$ [31]. The value of 161.4 eV for Bi $4f_{7/2}$ can be assigned to a Bi^{3+} oxidation state [31]. It is also found that the BE of Nb $3d_{5/2}$ is 209.1 eV, which confirms that Nb in the as-prepared samples exist in Nb^{5+} [31].

3.5. Photocatalytic activities

The photocatalytic activities of the $ABi_2Nb_2O_9$ (A=Sr, Ba) powders were investigated by the degradation of MO in aqueous solution under UV-light irradiation (λ=254 nm). Fig. 6 shows the concentration changes of MO at 464 nm as a function of irradiation time during the degradation process catalyzed by the $ABi_2Nb_2O_9$ (A=Sr, Ba) samples. The degradation rate of MO increases with the increase of the calcination temperature. This result indicates that the calcination temperature has a pronounced effect on the photocatalytic activities of $ABi_2Nb_2O_9$ (A=Sr, Ba). A good crystallinity can be obtained by annealing at high temperatures. It can decrease the recombination centers of photo-generated electrons and holes, and therefore can improve the catalytic activity of a photocatalyst [32]. As a result, the photocatalytic activities of the $ABi_2Nb_2O_9$ (A=Sr, Ba) samples are enhanced by increasing the calcination temperature. A large surface area is also essential for the photocatalytic decomposition of organic contaminants, due to that the absorption of an organic pollutant is the important process [29]. Therefore, the degradation rate of MO in the solution containing SBN-750 is faster than that of SBN-850 due to a large surface area of SBN-750 as mentioned in Section 3.1. Furthermore, the photocatalytic activities of the samples prepared by the citrate complex method are much higher than those of the samples synthesized via the solid state reaction, because the introduction of the solid state reaction which generally requires repeated mechanical mixing and a high-temperature process often gives rise to particle agglomeration with severe loss of effective surface area. Overall, the photocatalytic activities of $ABi_2Nb_2O_9$ (A=Sr, Ba) increase initially with the increase of calcination temperature due to the enhancement of the crystallinity, and then decrease because of the reduction of the surface area. This indicates that the photocatalytic activities of $ABi_2Nb_2O_9$ (A=Sr, Ba) were determined by the balance of the crystallinity and the surface area.

Furthermore, it is found that the photocatalytic reduction of MO can be well catalyzed by the $ABi_2Nb_2O_9$ (A=Sr, Ba) powders in the presence of N_2 and ammonium oxalate. Figs. 7 and 8 show the absorption peak of MO about 464 nm disappears rapidly and a new peak around 246 nm emerges, and it is contributed to the absorption of hydrazine [33]. XRD patterns of SBN-750 and BBN-850 before and after the catalytic test are shown in Fig. 9. It is found that the crystal structures of SBN-750 and BBN-850 are intact

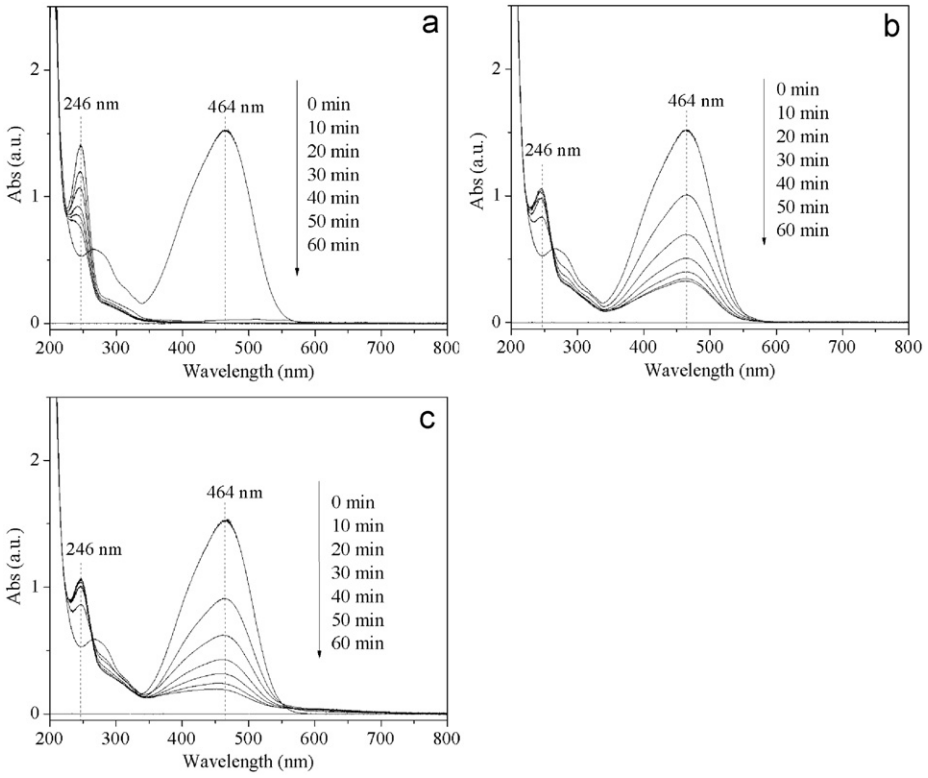

Fig. 7. UV–vis absorption spectral changes of MO during the photocatalytic reduction process catalyzed by (a) SBN-750, (b) BBN-850 and (c) Degussa P25.

during the catalytic test. Fig. 10 shows the variations in the concentration of MO catalyzed by SBN-750 under different conditions. No significant reaction of MO is observed either in the presence of SBN-750 bubbling with N_2 under UV-light irradiation (curve *b*), or in the presence of SBN-750 and ammonium oxalate under UV-light (curve c). However, MO discolors rapidly in the presence of SBN-750 and ammonium oxalate bubbling with N_2 under UV-light irradiation (curve *d*). Evidently, both ammonium oxalate and N_2 are indispensable for the photocatalytic reduction of MO in this experiment. Belloni and his co-workers [34] have found that the scavenging of photo-excited holes by HCO_2^- is faster than the electron–hole recombination or the trapping of unrecombined holes. Thus, ammonium oxalate is employed to trap photo-excited holes in this experiment. Furthermore, the formation of superoxide radicals through trapping photo-generated electrons by oxygen is suppressed significantly under an N_2 bubbling. Therefore, more electrons can escape from the pair recombination and are available to reduce MO to hydrazine, as shows in the next reaction [33]

$$(CH_3)_2NC_6H_4N{=}NC_6H_4SO^{3-} + 2H^+ + 2e^- \rightarrow (CH_3)_2NC_6H_4NHNHC_6H_4SO^{3-}$$

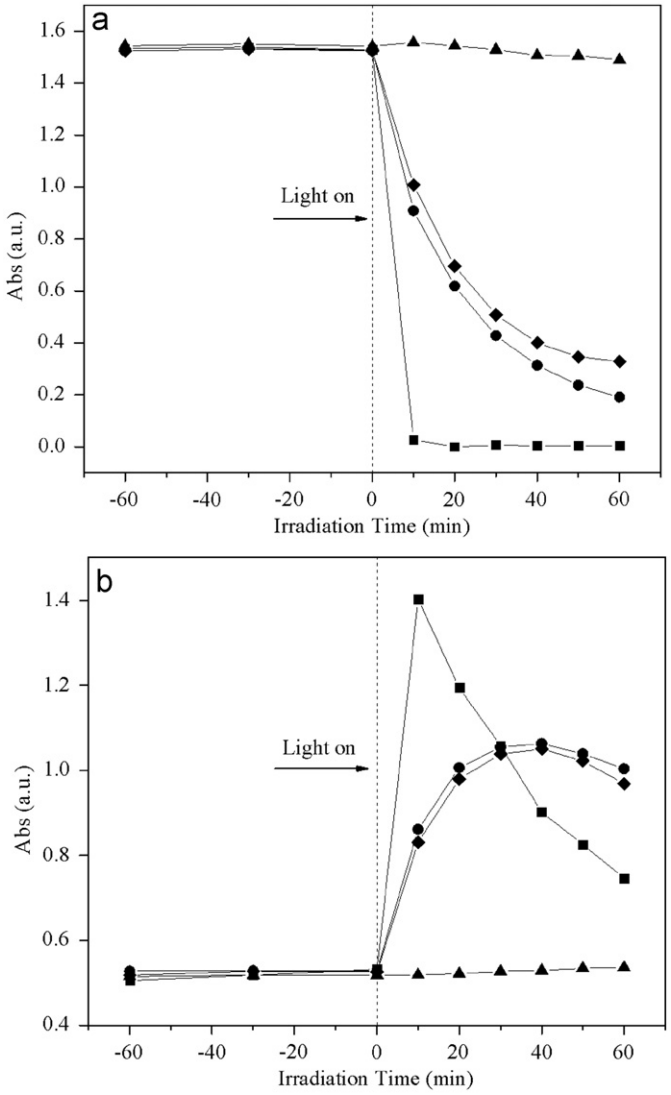

Fig. 8. Absorption changes at (a) 464 nm and (b) 246 nm during the photocatalytic reduction process (-■- SBN-750, -◆- BBN-850, -●- Degussa P25, -▲- without catalyst).

which only as an intermediate phase according to the decrease of the absorption peak around 246 nm. The remarkable process is reported for the first time, but the mechanism of this process has yet to be determined clearly. Thus, the photocatalytic reduction of MO catalyzed by the $ABi_2Nb_2O_9$ (A=Sr, Ba) photocatalysts in the presence of N_2 and ammonium oxalate will be analyzed in more detail in the next work for us.

$SrBi_2Nb_2O_9$ exhibits an excellent performance in the photocatalytic redox reaction of MO as compared to $BaBi_2Nb_2O_9$, which can be ascribed to a dipole moment in $SrBi_2Nb_2O_9$ crystal. The two oxides $ABi_2Nb_2O_9$ (A=Sr, Ba) as members of the $(M_2O_2)^{2+}(A_{m-1}B_mO_{3m+1})^{2-}$ family of compounds with m=2. In general, Aurivillius-type compounds consist of $(M_2O_2)^{2+}$ layers

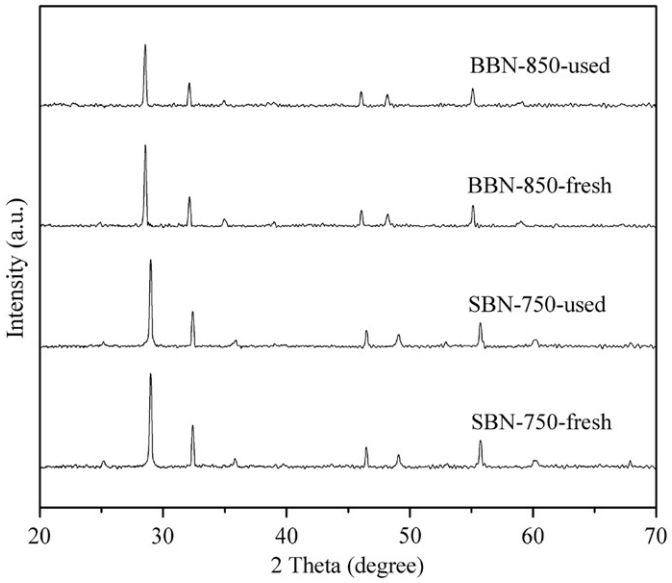

Fig. 9. XRD patterns of SBN-750 and BBN-850 before and after the photocatalytic reduction test.

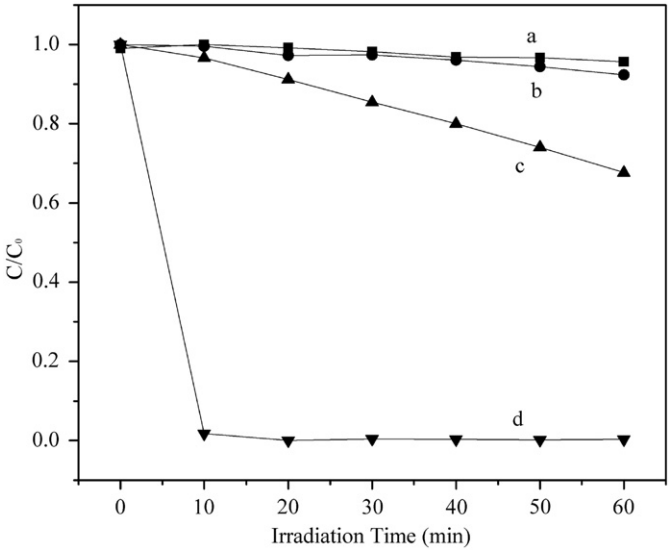

Fig. 10. Variations in the concentration of MO catalyzed by an SBN-750 under different conditions: (a) the blank experiment under UV-light irradiation, (b) in the presence of SBN-750 bubbling with N_2 under UV-light irradiation, (c) in the presence of SBN-750 with ammonium oxalate under UV-light irradiation, (d) in the presence of SBN-750 and ammonium oxalate bubbling with N_2 under UV-light irradiation.

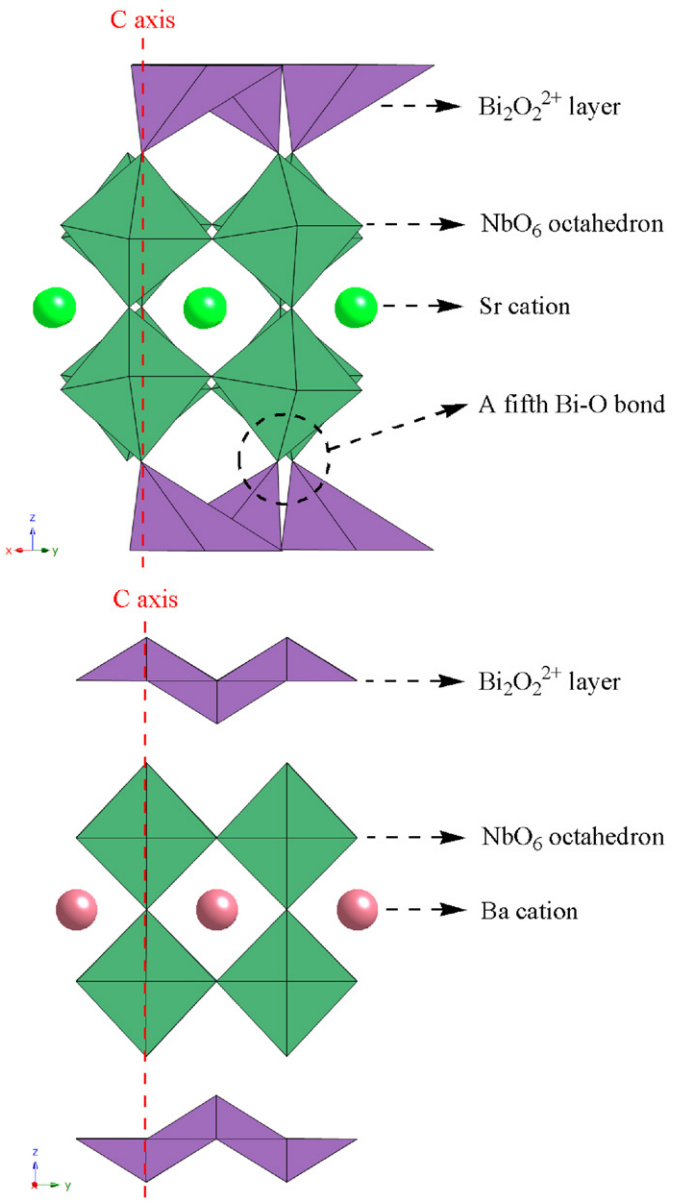

Fig. 11. Schematic structures of $ABi_2Nb_2O_9$ (A=Sr, Ba).

interleaved with $(A_{m-1}B_mO_{3m+1})^{2-}$ perovskite-type layers. However as shown in Fig. 11, stabilization of the perovskite-type layers often requires a tilting of the NbO_6 octahedra with respect to the c axis in $ABi_2Nb_2O_9$ (A=Sr, Ba) [17]. As a result, a fifth strong bond between Bi in the $Bi_2O_2^{2+}$ layers and O in the NbO_6 octahedra is found in $SrBi_2Nb_2O_9$ due to the NbO_6 octahedra tilting of 6°. In $BaBi_2Nb_2O_9$ crystal structure, the NbO_6 octahedra are tilted by less than 3° with respect to the c axis, because of the greater stability of the perovskite-type layers. The relatively small tilting of the NbO_6 octahedra in $BaBi_2Nb_2O_9$ results in a more regular Ba–O geometry. $SrBi_2Nb_2O_9$, which crystallizes in a polar space group, permits a dipole moment along perovskite layers (the c axis), due to the distortion of the framework of perovskite layers, whereas $BaBi_2Nb_2O_9$ does not. The dipole moment can enhance the separation of e^- and h^+ as the photo-excited electrons and holes are transferred in the crystal, and consequently can enhance the photocatalytic activity of $SrBi_2Nb_2O_9$ [35]. Therefore, $SrBi_2Nb_2O_9$ exhibits higher photocatalytic activity in the photocatalytic redox reduction of MO as compared to $BaBi_2Nb_2O_9$.

4. Conclusions

Microcrystalline $ABi_2Nb_2O_9$ (A=Sr, Ba) photocatalysts were successfully synthesized by a citrate complex method at a relatively low temperature as compared to the solid state reaction. Single-phase orthorhombic ($A2_1am$) SBN could be obtained after being calcined above 650 °C, while BBN adopted a tetragonal ($I4_1/mmm$) structure. Based on UV–vis DRS, the band gaps of the $ABi_2Nb_2O_9$ (A=Sr, Ba) powders were calculated to be around 3.34–3.54 eV. The photocatalytic activities of the as-prepared samples were investigated by the photocatalytic redox reaction of MO under UV-light irradiation (λ=254 nm) for the first time. SBN samples showed higher photocatalytic activities than those of BBN samples, due to the dipole moment in an SBN crystal. It was also found that the photocatalytic activities of $ABi_2Nb_2O_9$ (A=Sr, Ba) were determined by the balance of the crystallinity and the surface area.

Acknowledgments

The work was supported by National Natural Science Foundation of China (20777011), National Key Basic Research Program of China (973 Program: 2007CB613306) and Program for Changjiang Scholars and Innovative Research Team in University (PCSIRT0818).

References

[1] A. Moure, C. Alemany, L. Pardo, J. Eur. Ceram. Soc. 24 (2004) 1687.
[2] J.H. Bi, L. Wu, J. Li, Z.H. Li, X.X. Wang, X.Z. Fu, Acta Mater. 55 (2007) 4699.
[3] C. Belver, C. Adan, M. Fernandez-Garcia, Catal. Today 143 (2009) 274.
[4] Y. Shimodaira, H. Kato, H. Kobayashi, A. Kudo, J. Phys. Chem. B 110 (2006) 17790.
[5] L. Wu, J.H. Bi, Z.H. Li, X.X. Wang, X.Z. Fu, Catal. Today 131 (2008) 15.
[6] M. Shang, W.Z. Wang, S.M. Sun, L. Zhou, L. Zhang, J. Phys. Chem. C 112 (2008) 10407.
[7] H. Yin, A. Zhou, N. Chang, X. Xu, Mater. Res. Bull. 44 (2009) 377.
[8] H.G. Kim, D.W. Hwang, J.S. Lee, J. Am. Chem. Soc. 126 (2004) 8912.
[9] J.H. Bi, L. Wu, Z. Li, X.X. Wang, X.Z. Fu, Mater. Lett. 62 (2008) 155.
[10] B. Muktha, M.H. Priya, G. Madras, T.N.G. Row, J. Phys. Chem. B 109 (2005) 11442.
[11] Y.X. Li, G. Chen, H.J. Zhang, Z.S. Lv, J. Int., Hydrogen Energy 35 (2010) 2652.
[12] Q.D. Zhou, B.J. Kennedy, Chem. Mater. 15 (2003) 5025.
[13] L. Zhou, W.Z. Wang, L.S. Zhang, J. Mol. Catal. A: Chem. 268 (2007) 195.
[14] L.J. Xie, J.F. Ma, G.J. Xu, Mater. Chem. Phys. 110 (2008) 197.
[15] C.X. Xu, X. Wei, Z.H. Ren, Y. Wang, G. Xu, G. Shen, G.R. Han, Mater. Lett. 63 (2009) 2194.
[16] Ismunandar, B.J. Kennedy, J. Mater. Chem. 9 (1999) 541.
[17] Ismunandar, B.J. Kennedy, Gunawan Marsongkohadi, J. Solid State Chem. 126 (1996) 135.
[18] J.H. Yi, P. Thomas, M. Manier, J.P. Mercurio, I. Jauberteau, R. Guinebretieere, J. Sol–Gel Sci. Technol. 13 (1998) 885.
[19] S.P. Gaikwad, S.R. Dhage, H.S. Potdar, V. Samuel, V. Ravi, J. Electroceram. 14 (2005) 83.
[20] S.P. Gaikwad, H.S. Potdar, V. Samuel, V. Ravi, Ceram. Int. 31 (2005) 379.
[21] Z.J. Li, R.Q. Liu, Y.H. Xie, S. Feng, J.D. Wang, Solid State Ionics 17 (2005) 1063.
[22] G.K. Zhang, J.L. Yang, S.M. Zhang, Q. Xiong, B.B. Huang, J.T. Wang, W.Q. Gong, J. Hazard. Mater. 172 (2009) 986.
[23] Y.Y. Zhou, Z.F. Qiu, M.K. Lu, Q. Ma, A.Y. Zhang, G.J. Zhou, H.P. Zhang, Z. Yang, J. Phys. Chem. C 111 (2007) 10190.
[24] D. Nelis, K. Werde, D. Mondelares, G. Vanhoyland, H. Vandenrul, M.K. Vanbael, J. Mullens, L.C. Vanpoucke, J. Sol–Gel Sci. Technol. 26 (2003) 1125.
[25] S.M. Zanetti, E.I. Santiago, L.O.S. Bulhoes, J.A. Varela, E.R. Leite, E. Longo, Mater. Lett. 57 (2003) 2812.
[26] D. Nelis, D. Mondelaers, G. Vanhoyland, A. Hardy, K.V. Werde, H.V.D. Rul, M.K.V. Bael, J. Mullens, L.C.V. Poucke, J. D'Haen, Thermochim. Acta 426 (2005) 39.
[27] Y. Narendar, G.L. Messing, Chem. Mater. 9 (1997) 580.
[28] W.J. Wang, J.H. Bi, L. Wu, Z.H. Li, X.Z. Fu, Scr. Mater. 60 (2009) 186.
[29] A. Kudo, Y. Miseki, Chem. Soc. Rev. 38 (2009) 253.
[30] H. Van Doveren, J.A.T.H. Verhoeven, J. Electron. Spectrosc. Relat. Phenom. 21 (1980) 265.
[31] C.D. Wagner, W.M. Riggs, L.E. Davis, J.F. Moulder, G.E. Muilenberg, Handbook of X-ray Photoelectron Spectroscopy, Eden Prairie, Minnesota, 1978.
[32] G.H. Tian, H.G. Fu, L.Q. Jing, C.G. Tian, J. Hazard. Mater. 161 (2009) 1122.
[33] M. Yoon, M. Seo, C. Jeong, J.H. Jang, K.S. Jeon, Chem. Mater. 17 (2005) 6069.
[34] J. Belloni, M. Treguer, H. Remita, R.D. Keyzer, Nature 402 (1999) 865.
[35] A. Kudo, H. Kato, S. Nakagawa, J. Phys. Chem. B 104 (2000) 571.